

Identifying Autism Spectrum Disorder From Resting-State fMRI Using Deep Belief Network

Zhi-An Huang^{ID}, Zexuan Zhu^{ID}, Senior Member, IEEE, Chuen Heung Yau, and Kay Chen Tan^{ID}, Fellow, IEEE

Abstract—With the increasing prevalence of autism spectrum disorder (ASD), it is important to identify ASD patients for effective treatment and intervention, especially in early childhood. Neuroimaging techniques have been used to characterize the complex biomarkers based on the functional connectivity anomalies in the ASD. However, the diagnosis of ASD still adopts the symptom-based criteria by clinical observation. The existing computational models tend to achieve unreliable diagnostic classification on the large-scale aggregated data sets. In this work, we propose a novel graph-based classification model using the deep belief network (DBN) and the Autism Brain Imaging Data Exchange (ABIDE) database, which is a worldwide multisite functional and structural brain imaging data aggregation. The remarkable connectivity features are selected through a graph extension of K -nearest neighbors and then refined by a restricted path-based depth-first search algorithm. Thanks to the feature reduction, lower computational complexity could contribute to the shortening of the training time. The automatic hyperparameter-tuning technique is introduced to optimize the hyperparameters of the DBN by exploring the potential parameter space. The simulation experiments demonstrate the superior performance of our model, which is 6.4% higher than the best result reported on the ABIDE database. We also propose to use the data augmentation and the oversampling technique to identify further the possible subtypes within the ASD. The interpretability of our model enables the identification of the most remarkable autistic neural correlation patterns from the data-driven outcomes.

Index Terms—Autism spectrum disorder (ASD), computational diagnostic model (CDM), deep belief network (DBN), functional connectivity (FC), functional magnetic resonance imaging (fMRI).

Manuscript received September 17, 2019; revised April 4, 2020; accepted July 4, 2020. Date of publication July 21, 2020; date of current version July 7, 2021. This work was supported in part by the National Natural Science Foundation of China (NSFC) under Grant 61876162 and Grant 61871272, in part by the Shenzhen Scientific Research and Development Funding Program under Grant JCYJ20180307123637294 and Grant JCYJ20190808173617147, and in part by the Research Grants Council of the Hong Kong SAR under Grant CityU11202418 and Grant CityU11209219. (*Corresponding authors:* Zexuan Zhu; Kay Chen Tan.)

Zhi-An Huang and Kay Chen Tan are with the Department of Computer Science, City University of Hong Kong, Hong Kong, and also with the Shenzhen Research Institute, City University of Hong Kong, Hong Kong (e-mail: zahuang2-c@my.cityu.edu.hk; kaytan@cityu.edu.hk).

Zexuan Zhu is with the College of Computer Science and Software Engineering, Shenzhen University, Shenzhen 518060, China, also with the Shenzhen Pengcheng Laboratory, Shenzhen 518055, China, and also with the SZU Branch, Shenzhen Institute of Artificial Intelligence and Robotics for Society, Shenzhen University, Shenzhen 518060, China (e-mail: zhuzx@szu.edu.cn).

Chuen Heung Yau is with the School of Chinese Medicine, The University of Hong Kong, Hong Kong (e-mail: annyau333@gmail.com).

Color versions of one or more of the figures in this article are available online at <https://ieeexplore.ieee.org>.

Digital Object Identifier 10.1109/TNNLS.2020.3007943

I. INTRODUCTION

AUTISM spectrum disorder (ASD) is a range of common childhood neurodevelopmental disorders including autism, Asperger's syndrome, and other related conditions. The individuals with ASD typically present with variable deficits of clinical syndromes in restrictive interests, social communication, and repetitive behaviors. The rising incidence of ASD has attracted public concern. The serious impairments of ASD can last throughout one's life and represent a major burden of health and finance globally. The lifetime costs of treating an ASD patient in the United States has exceeded one million dollars [1]. Early treatments and intervention can alleviate the symptoms and improve the quality of the life of the patients. Although the neurogenetics and neurobiology of the ASD have been widely investigated, the pathology of the ASD still remains uncertain. Due to the etiological heterogeneity of the ASD, no neuropathological or unified structural traits have been conclusively characterized [2]. The symptom-based diagnostic criteria are still fundamental for the clinical diagnosis of the ASD. The ASD patients are typically diagnosed by using the criteria checklist of the diagnostic and statistical manual (DSM). Despite the everchanging diagnostic metrics and categories over the past decades, the diagnosis of ASD, at its core, still suffers from significant limitations in the observational strategies. The recent studies have revealed that disparities between the individuals with autism and those without autism have reduced over time, which could be attributed to the continuous changes in the definition of autism [3]. In other words, the traditional clinical diagnosis could more likely lead to misdiagnosis due to the subjectivity and complexities involved in the diagnosis process. In addition, the global shortfall in the well-qualified professionals of ASD could delay the early diagnosis and treatment by aggravating the related symptoms.

The noninvasive neuroimaging techniques provide data for capturing the neural patterns of the brain structure and function. As a kind of neuroimaging techniques, functional magnetic resonance imaging (fMRI) [4] is extensively employed to investigate the functional variations and structural alterations in the autistic brain activity. The rationale of fMRI is to measure the blood-oxygen-level-dependent (BOLD) contrast related to the energy use by the brain cells. Resting state fMRI (rs-fMRI), serving as one of the fMRI paradigms, provides the data of the subjects' baseline BOLD variance. Numerous studies have proven the feasibility of using rs-fMRI

to uncover the pairwise interactions between the regions of interest (ROIs) in psychiatric illnesses such as Alzheimer disease [5], attention-deficit hyperactivity disorder (ADHD) [6], autism [7], and others [8]. Rs-fMRI signals have shown great potential in identifying the neuropathology diagnostic biomarkers [9]. Leveraging the data integrated from multiple data sets could be a silver-bullet solution for clinical applications through sharing and consolidating independent data samples across different studies. This can greatly contribute to the diagnosis, determination of risk prognosis, and monitoring of the treatment response of the ASD [10]. However, controversies still surround the preprocessing pipelines including bandpass filtering and global signal regression. Without a unified set of standard, the data-aggregation solution could be debatable with regard to the reproducibility and generalizability of the data sources. Uncontrolled variations can inevitably exist in the intersite data ranging from MRI-acquisition protocols (e.g., MRI vendors, flip angle, scan time, and basic pulse sequence parameters), to recruitment strategies (e.g., age tendency and IQ-range), and to participant instructions (e.g., eye open/closed conditions) [11]. This impedes the effort to leverage the aggregated MRI data in research. The advances in computing power and methodology [12] have enabled the development of the useful computational model to solve the aforementioned issues.

In this article, we propose a novel graph-based classification model using the deep belief network (DBN) [13]. To train our model, we leverage the data of the Autism Brain Imaging Data Exchange (ABIDE) database, which is a worldwide multisite functional and structural brain imaging data aggregation [14]. First, the ASD remarkable functional connectivities (FCs) are selected by the graph-based feature-selection (GBFS) method based on both external and internal measures. Then, a restricted path-based depth-first search (RP-DFS) algorithm is implemented to explore further the topological information implied on the graph. Finally, a three-layer DBN with automatic hyperparameter tuning is proposed for the identification of the ASD patients. The result of the mean accuracy of 0.764 ± 0.022 based on tenfold cross validation (CV) shows that our model outperforms the state-of-the-art methods. The receiver-operating-characteristic (ROC) curve and the area under ROC curve (AUC) are used to evaluate the classification performance for the best case and worst case scenarios. The leave-one-site-out test well demonstrates the applicability and generalization of the proposed model to a new different site. The proposed model is also demonstrated to have moderate improvement in predictive capability for identifying the ASD subtypes. No significant differences are observed between accuracy and the confounding factors, e.g., age, gender, and full-scale intelligence quotient (FIQ) scores. In addition, the interpretability of our model enables a statistical analysis for uncovering the correlation patterns in the autistic brains. Subsequently, some rules that we found are presented in this work. The main contributions of this article can be summarized as follows.

- 1) The GBFS method is proposed to select effectively the remarkable connections in the ASD brain based on both external and internal measures. Moreover, we further

design a DBN classifier with automatic hyperparameter tuning, which is more accurate and efficient than the other state-of-the-art algorithms.

- 2) We first try to identify possible subtypes within the ASD on the imbalanced rs-fMRI data sets. To tackle this issue, data augmentation and oversampling technique are introduced based on the proposed model. The experimental results suggest that our work obtains moderate improvement in predictive capability for identifying the ASD subtypes.
- 3) Based on the real-world data of ABIDE, we conduct a series of comprehensive experiments to validate the superior performance of our model against the state-of-the-art methods. The interpretability of our model enables us to prioritize the seminal correlation patterns in the autistic brains, some of which have been manually validated by the published literatures.

The rest of this article is organized as follows. Section II reviews the related work. Section III describes the proposed framework including the GBFS, RP-DFS, and DBN models with automatic hyperparameter tuning. The experimental results and analysis are discussed in Section IV. Finally, Section V concludes this article.

II. RELATED WORK

More recently, there has been an increasing interest to investigate brain FC as neurological biomarkers in numerous studies for the classification of mental states (e.g., the presentation of emotions [15], learning [16], and semantic categories [17]) and mental disorders (e.g., ASD, schizophrenia, and major depressive disorder (MDD) [18]). Based on the discovery of neurological biomarkers, extensive efforts have been made to developing the computer-aided diagnostic models [19]–[21]. In the following, we briefly review some extensively used feature-selection strategies and classification models based on brain disorder studies.

A. Feature-Selection Strategies

To select the discriminative and effective features on the fMRI data is particularly important to well-performing classifiers for the identification of mental disorder [23]. Especially, for the FCs, usually tens of thousands of features are defined, whereas only a small percentage of them carry valuable information toward the goal. Nielsen *et al.* [24] extracted 7265 features from 26.4 million connections by computing the pairwise correlation coefficient between each generated ROI. The feature-selection strategies can be mainly categorized into three classes: filter methods, wrapper methods, and embedded methods [25].

Filter methods are widely applied for feature selection thanks to their effectiveness in computational expense and their robustness to overfitting. The basic principle is to assign proxy measures (e.g., statistical test [25], Fisher score [26], and correlation coefficient [27]) to the features using the general characteristics of the data sets, so as to harvest the optimal feature subsets with top scores. The group-level statistical test is the most popular type of filter methods such as *t*-test, ranksum-test, and Welch's *t*-test. The primary issue with this strategy is

that remarkable features are selected by their *p*-values, which sometimes disable to reflect those with the largest discrimination power. That is, features with small *p*-values (i.e., high confidence) might result in a poor classification performance [28]. Correlation-based feature selection is another type of filter methods to rank the features based on the assumption that optimal feature subsets contain highly correlated information with regard to the classification so as to distinguish between the instances [27]. Abraham *et al.* use a regularized covariance estimator to estimate the connectivity coefficients between the ROI time series based on three different measure methods [11]. This strategy can achieve satisfactory performance thanks to the low-order polynomial runtime, applicability to the binary or continuous data, as well as noise-tolerance and robustness to the FC feature interactions.

Wrapper methods select decreasing numbers of features with different possible combinations depending on the performance of the classifiers. Recursive feature elimination (RFE) [29] and genetic algorithm (GA) [30] are two extensively used wrapper methods to produce seminal feature combinations. RFE optimizes classifiers by recursively considering smaller and smaller possible feature combinations. To explore an optimal subset of features, the work in [31] determines the number of feature variables for classification by the highest accuracy as recursively increasing the thresholds at seven different effect sizes. GA initializes binary encoded populations (representing a feature included or not) and then generates high-quality feature combinations by the bioinspired operators, i.e., mutation, crossover, and selection. The third class, embedded methods are quite similar to the wrapper methods, since they also integrate feature selection into the learning of specific classifiers for the decision processes. The major difference from the wrapper methods is that an intrinsic model building metric is leveraged during learning. The least absolute shrinkage and selection operator (LASSO) method is the most popular embedded method to add a penalty against complexity for reducing the degree of variance or overfitting of a linear model [32]. In recent neuroimaging studies [33], [34], multitask feature selection as an emerging approach aims to integrate data sharing highly consistent feature patterns between the modalities by ideally ignoring the data-dependent noise. Based on sparse learning, Wang *et al.* [35] used the group $\ell_{2,1}$ -norm regularizer to impose the sparsity between all features and nonsparsity between the tasks for obtaining important features. In theory, wrapper methods and embedded methods tend to yield better feature subsets specific for a particular classifier than filter methods do. However, the quantity of possible feature combinations exponentially grows, as the number of features increases. Wrapper methods and embedded methods are more computationally expensive than the filter methods due to the repeated learning steps and cross-validation. Furthermore, the features selected by them could not well characterize the reproducible autistic connectivity patterns due to their dependent relationships with specific classifiers. Since the purpose of this study is to explore reproducible biomarkers with discriminative power for effective classification, a heuristic graph-based filter feature-selection method is proposed

based on both external and internal measures on the rs-fMRI data.

B. Classification Models

In the previous literature [20], [24], traditional machine-learning (ML) classifiers with the hand-engineered features are commonly used to uncover the autistic function patterns. The ongoing development of the ML toolkits (e.g., scikit-learn [36]) provides easy-to-implement ML methods and allows researchers to compare the feasibility and effectiveness of the diverse ML methods, such as random forest (RF) and SVM [37]. Plitt *et al.* explored nine ML classification algorithms based on the statistical significance of accuracy, positive predictive value (PPV), and negative predictive value (NPV) [19]. However, most ML classifiers rely on the “shallow” or linear models. They are incapable of capturing the topological information within the brain networks as well as the relationships between the connectivity features and the clinical traits, especially on the large-scale data sets [38].

In recent years, deep-learning (DL) techniques [39], [40] have emerged as a promising approach with an outstanding performance comparable with or even in some cases superior to human experts. A growing number of studies [31], [40], [41] attempt to employ DL algorithms for the classification of brain disorders and address the issues of generalizability and subjectivity brought by the ML classifiers. Heinsfeld *et al.* [39] concluded that DL algorithms should minimize the human intervention to extract automatically the relevant features using unsupervised learning methods. They use two stacked denoising autoencoders to transfer 19 900 features into the deep neural network (DNN) [42], achieving the average accuracy of 70%, which is the best result reported to date using the whole ABIDE database. The well-performing DL classifiers benefit from their hierarchical structure with different levels of complexity and nonlinear transformations with different levels of abstraction provided by the hidden layers [25], [43]. This allows us to characterize the reproducible autistic connectivity patterns or “fingerprints” served as biomarkers, to discriminate effectively the ASD patients from the control. Nevertheless, determining appropriate models’ configuration setting is quite challenging by the many hyperparameter choices one must make, e.g., learning rates and batch sizes. The automatic hyperparameter-tuning technique is of crucial importance for using the DL algorithms in practice. In this work, we propose a three-layer DBN model with the automatic hyperparameter-tuning technique for classification and further improve the accuracy through tackling this issue.

III. MODEL DESIGN

The flowchart of the proposed model is shown in Fig. 1. First, by the preprocessing pipeline, the mean time series of the ROIs are extracted from the raw rs-fMRI data and then converted into 2-D feature matrices T , where T_{ik} represents the i th ROI’s mean time series of the k th timestamp. GBFS is used to select remarkable autistic functional connections for graph construction based on both external and internal measures. Then, we exploit the topological information to enrich the

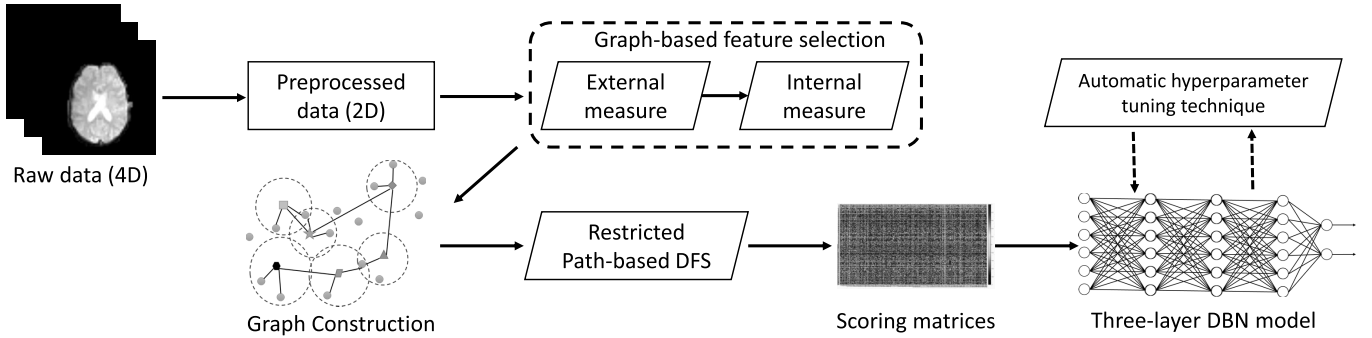


Fig. 1. Flowchart of the proposed model.

graph representation by using the RP-DFS method. Finally, a three-layer DBN model is built and its configuration setting is optimized by automatic hyperparameter tuning.

A. Graph-Based Feature Selection

In this section, the GBFS is proposed to select the remarkable autistic functional connections based on the preprocessed data sets. Incorporating appropriate FC features is necessary for the classification of brain disorders. If we calculate all FCs between the voxels, the number of features adds up to tens of thousands. The irrelevant features with redundant information would be detrimental to the classification performance. In this work, the Pearson correlation coefficient (PCC) is used to measure the levels of coactivation between each ROI's time series as follows:

$$\text{FC}(i, j) = \frac{\sum_{k=1}^N (T_{ik} - \bar{T}_i)(T_{jk} - \bar{T}_j)}{\sqrt{\sum_{k=1}^N (T_{ik} - \bar{T}_i)^2 \sum_{k=1}^N (T_{jk} - \bar{T}_j)^2}} \quad (1)$$

where N represents the total number of timestamp and varies from different institutes. $\text{FC}(i, j)$ means the FC correlation between any two ROIs ranging from 1 (highly correlated) to -1 (highly anticorrelated). In this way, the generated connectivity vector for each subject contains 19900 features/connections [200 ROIs, $(200 \times (200 - 1)/2) = 19900$]. The remarkable autistic connections of the ROIs are selected based on both external and internal measures.

First, the external measure is a data-driven approach for globally identifying the unique neural patterns associated with ASD. As mental disorders can be considered as disturbances or disruptions of the normal operation of brain activity, the remarkable connections need to satisfy the following two criteria. First, remarkable connections must be distinctive enough in terms of autistic average level. All ASD data sets are merged to calculate the mean value for each connection, denoted as $\text{mean}(\text{FC}_{\text{ASD}})$, and the global mean value, denoted as mean_{ASD} , as well as the global standard deviation (STD) as STD_{ASD} from all connections. Then, those connections with $\text{mean}(\text{FC}_{\text{ASD}}(i, j))$ higher or lower than mean_{ASD} for α -times STD_{ASD} are considered to satisfy this condition. A default filter factor α is used to control the number of selected connections. Second, remarkable connections must be simultaneously discriminative between the ASD group and the typical control (TC) group. In other words, combined with the first criteria, the selected connections should be remarkable

in the ASD group, while unremarkable in the TC group. Accordingly, these two criteria can be mathematically subject to

$$\begin{cases} \|\text{mean}(\text{FC}_{\text{ASD}}(i, j)) - \text{mean}_{\text{ASD}}\| > \alpha * \text{STD}_{\text{ASD}} \\ \|\text{mean}(\text{FC}_{\text{TC}}(i, j)) - \text{mean}_{\text{TC}}\| \leq \alpha * \text{STD}_{\text{TC}}. \end{cases} \quad (2)$$

α is empirically set to 1 in our work by tenfold CV. Each connection is examined to determine whether it should be selected as a remarkable connection based on these two criteria. As such, only 81 qualified connections are selected to perform the internal measure in the next step. It is worth to note that when we repeat the same procedures for the TC group based on the opposite version of (2), the remarkable connections of the TC group, which are remarkable in the TC group while unremarkable in the ASD group, achieve up to 380 (as shown in Fig. 2). The brain networks for both ASD and TC groups are visualized in Fig. 3 using the BrainNet Viewer [44]. Most notably, 115 and 37 remarkable connections in the TC group are associated with the frontal and posterior cortical areas, respectively. Whereas in the ASD group, only 18 and 4 remarkable connections are associated with the frontal and posterior cortical areas, respectively. This finding is consistent with the theory of frontal-posterior underconnectivity in autism [45], which attributes the disorder to lower the synchronization caused by lower communication bandwidths between the frontal and posterior areas in the autistic brain. Therefore, the external measure can explore the reproducible neurological biomarkers with discriminative power in deciphering remarkable autistic neural correlation patterns from the data-driven outcomes.

Second, a graph extension of K -nearest neighbors as an internal measure is applied for graph construction on the communities of potential ROIs between those remarkable connections selected by the external measure. As shown in Fig. 4, this approach takes advantage of the spatial distribution information by detecting the normalized neighborhood of the K -nearest ROIs as the “receptive fields” for the connected communities. For a target remarkable connection, their neighbor ROIs do not belong to this remarkable connection. Taking the diamond-shaped node (denoted as Node_d) and the triangle-shaped node (denoted as Node_t) in Fig. 4 as examples, a graph is initialized with edges connecting Node_t and Node_d . We assume that the autistic neuronal activity could function as the collaborative activation pattern in the potential

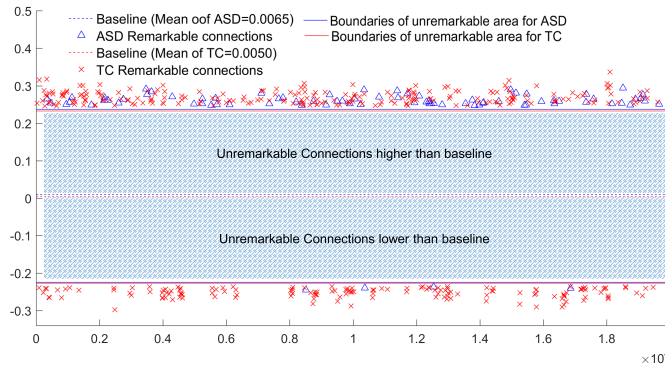


Fig. 2. 81 and 380 remarkable connections are highlighted in the ASD and TC groups, respectively ($STD_{ASD} = 0.2407$ and $STD_{TC} = 0.2437$).

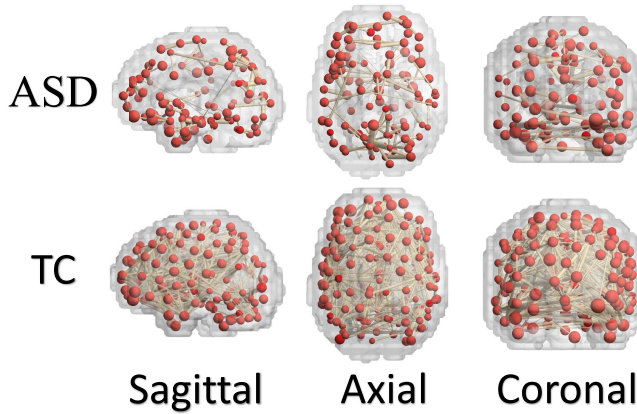


Fig. 3. Visualization of brain networks for the ASD and TC groups from the views of the sagittal, axial, and coronal planes.

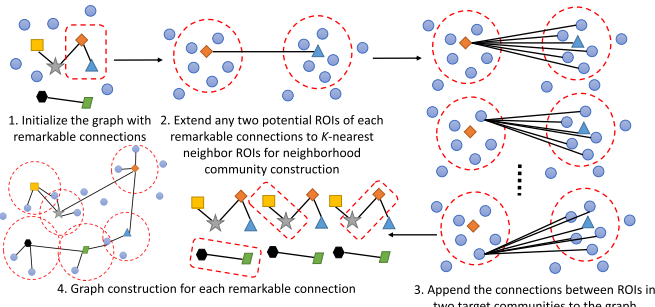


Fig. 4. Illustration of the internal measure pipeline by a graph extension of K -nearest neighbors.

associated areas, rather than the single region-to-region connectivity interaction. The subgraph extension is conducted by extending both $Node_t$ and $Node_d$ to their K -nearest neighbor ROIs forming communities (subgraphs) based on Euclidean distance. The FCs of the ROIs between the subgraphs of $Node_t$ and $Node_d$ are appended to the graph with their weights that are estimated by the PCC. After using GBFS for each remarkable connection, the number of selected FC features should be $81 \times (K + 1)^2 = 3969$, where K is empirically set to 6 in this work. After filtering out 681 repeated connections, we only consider 16.52% ($3288/19\,900 \times 100\%$) of the original features associated with the autistic brain activity. The pseudocode is shown in Algorithm 1.

Algorithm 1 Pseudocode of GBFS

Input: The # of nearest neighbors K , a feature matrix T .

Output: Graph $G(V, E)$.

```

1: Initialize remarkable connection set  $\mathcal{S} = \{\}$ 
2: Split all data sets into ASD group and TC group
3: Calculate  $mean(FC_{ASD})$ ,  $mean_{ASD}$ , and  $STD_{ASD}$  in
   ASD group as well as  $mean(FC_{TC})$ ,  $mean_{TC}$ , and
    $STD_{TC}$  in TC group
4: for  $i = ROI_1, \dots, ROI_{200}$  do
5:   for  $j = i + 1, \dots, ROI_{200}$  do //19,900 in total
6:     if  $FC(i, j)$  satisfies formula (2) then
7:        $\mathcal{S} \leftarrow \mathcal{S} \cup edge(i, j)$  //add remarkable links
8:     end
9:   end
10: end //End of the external measure
11: Initialize Graph  $G: G(V, E) = \emptyset$ 
12: for each  $edge(i, j) \in \mathcal{S}$  do
13:   Pick  $K$ -nearest neighbor ROIs for  $i, j$  as  $U_i, U_j$ 
14:   for each ROI  $p \in U_i$  do
15:     for each ROI  $q \in U_j$  do
16:       if  $edge(p, q) \notin G$  then
17:          $edge(p, q).weight \leftarrow FC(p, q)$ 
18:          $G.V \leftarrow G.V \cup \{p, q\}$  //add nodes
19:          $G.E \leftarrow G.E \cup edge(p, q)$  //add edges
20:       end
21:     end
22:   end
23: end //End of the internal measure

```

B. Restricted Path-Based Depth-First Search Algorithm

The network topology in the graph is helpful to unravel the implied information, which effectively enriches the connectivity matrices. We extend our previous work [46] and redesign a restricted path-based depth-first search algorithm named RP-DFS for refining the FC feature matrices to traverse all potential paths between both target ROIs of each remarkable connection. A path (denoted as P) is defined as a set of connections between two target ROIs within restricted lengths (steps). Given two target ROIs as R_i and R_j , this algorithm is mainly based on two assumptions. First, if R_i and R_j are connected with another ROI R_k , denoted as $R_i \leftrightarrow R_k$ and $R_j \leftrightarrow R_k$, but disconnected with each other, R_i and R_j are considered to have a semiremarkable connection in graph with a weight that should be relatively reduced as the path elongates. Second, the more the restricted paths are found to connect the two target ROIs, the more likely they have a strong correlation. The accumulative contributions are integrated from all potential paths between R_i and R_j as a final score. The score can be formulated as

$$\text{score}(R_i, R_j) = \sum_{t=1}^{N_{ij}} \left(\prod_{l=1}^{t-1} W(P_l) \right)^{F_{\text{decay}}(P_t)} \quad (3)$$

$$F_{\text{decay}}(P) = \beta \times (\text{len}(P) - 1) \quad (4)$$

where N_{ij} is the maximum restricted length of P between R_i and R_j , β is the decay factor ranging from 1.5 to 3 according

to the previous research [47], $W(P_t)$ represents the weight of the t th connection in path P , and $F_{\text{decay}}(P)$ is the exponential decay function assigning less confidence to the longer paths. This algorithm is easy to implement as a recursive computation. The principle of acyclicity ensures that no ROIs are repeatedly visited in each restricted path. Considering the computational complexity, the maximum length of paths is set to 2 (i.e., $N_{ij} = 2$) in this work. Besides those 3288 remarkable connections like $R_i \leftrightarrow R_k$, there are 7712 semiremarkable connections like $R_i \leftrightarrow R_k \leftrightarrow R_j$ explored by this algorithm. As such, total 125 639 potential paths are involved in the remarkable and semiremarkable connections in the graph for each data set. The final scores of the involved connections ($3288 + 7712 = 11\,000$) are converted into a 2-D matrix of size 110×100 for classification. The algorithm is shown in Algorithm 2.

Algorithm 2 Pseudocode of RP-DFS

Input: Graph $G(V, E)$, Max_len
Output: A scoring matrix T' .

- 1: Initialize a scoring matrix T' and a path set PS
- 2: **for** $\text{len}=1,\dots,\text{Max_len}$ **do**
- 3: **for** each $\text{Node}_i \in G.V$ **do**
- 4: **for** each $\text{Node}_j \in G.V$ **do**
- 5: $PS_{ij} \leftarrow \text{getAllPaths}(\text{Node}_i, \text{Node}_j, G(V, E), \text{len})$
- 6: **for** each path $\in PS_{ij}$ **do**
- 7: $T' \leftarrow T' + \text{Score}(\text{Node}_i, \text{Node}_j)$ via Eq.3 & 4
- 8: **end**
- 9: **end**
- 10: **end**
- 11: **end**
- 12: //define function
- 13: **getAllPaths**(Origin_Node , Target_Node , $G(V, E)$, len):
- 14: **return** **allPaths**(Target_Node , $\text{list}(\text{Origion_Node})$,
 $\text{set}(\text{Origin_Node})$, $G(V, E)$, $\text{list}()$, len)
- 15: //define function
- 16: **allPaths**(Target_Node , currentPath , used_Nodes ,
 $G(V, E)$, answerPath , len):
- 17: $\text{Last_Node} \leftarrow$ the last node of currentPath
- 18: **if** $\text{Last_Node}=\text{Target_Node}$ **then**
- 19: $\text{answerPath} \leftarrow \text{answerPath} \cup \text{currentPath}$
- 20: **else**
- 21: **for** each $\text{Neighbor_Node} \in G.V(\text{Last_Node})$ **do**
- 22: **if** $\text{Neighbor_Node} \notin \text{used_Nodes}$ **and**
 $\text{currentPath}.len() < \text{len}$ **then**
- 23: $\text{currentPath} \leftarrow \text{currentPath} \cup \text{Neighbor_Node}$
- 24: $\text{used_Nodes} \leftarrow \text{used_Nodes} \cup \text{Neighbor_Node}$
- 25: $\text{allPaths}(\text{Target_Node}, \text{currentPath}, \text{used_Nodes},$
 $G(V, E)$, answerPath , len) //recursion
- 26: $\text{used_Nodes} \leftarrow \text{used_Nodes} \setminus \text{Neighbor_Node}$
- 27: $\text{currentPath.pop}()$
- 28: **end**
- 29: **end**
- 30: **return** answerPath

C. DBN Model With Automatic Hyperparameter Tuning

Based on the refined feature matrices, DL models are capable of automatically learning the optimal representation for the identification of ASD. In this section, we use a three-layer DBN model with the automatic hyperparameter-tuning technique for classification (see Fig. 5). As one of the most effective DL models [13], the DBN is composed of three restricted Boltzmann machine (RBM) [48] layers of hidden units with communications between the concatenated layers but not between the units for each layer. Basically, the training of the DBN performs in two stages: unsupervised pretraining and supervised fine-tuning [49]. First, in the unsupervised pretraining, the layers of DBN iteratively learn to reconstruct probabilistically the visible units without labels. The activation functions of the visible layers and of the hidden layers in the RBMs are set to the affine function and sigmoid functions, respectively. Then, the supervised learning of the DBNs fine-tunes the resulting network with labels using the root-mean-square propagation (RMSProp) [50] and momentum technique as the backpropagation methods, where the activation function is the rectified linear unit (ReLU) [51]. The outputs are derived from the softmax function, yielding the probability of being one class (i.e., ASD or TC). Hence, there are only two units in the output layer based on one-hot encoding. To calculate the difference between the estimated and true values, both unsupervised and supervised learnings employ the same loss function, i.e., the cross entropy. Dropout regularization is used for reducing overfitting.

The well-known issue of using DL in classification is the strenuous and time-consuming hyperparameter tuning, which varies from different problems. Feature reduction leads to the hierarchical structure with lower levels of computational complexity that shortens the training time based on the GPU acceleration. The automatic hyperparameter-tuning technique is first introduced for the computational diagnosis of mental disorders using Bayesian optimization (BO) with Gaussian processes (GPs) [52]. Thanks to its useful surrogate model and good practices, we take the advantages of speed to increase the number of iterations for further improving the classification accuracy. The BO-based optimizer is used to guide the potential search direction toward the seminal hyperparameter sets in the problem space. Three continuous and four discrete hyperparameter values shown in Fig. 5 are optimized. Based on [53], we consider mathematically the problem of seeking a global maximizer of an unknown objective function f as

$$x^* = \arg \max_{x \in \mathcal{X} \subseteq \mathbb{R}^d} f(x) \quad (5)$$

where \mathcal{X} is the certain design space of interest in global optimization. Since f is unknown, the sequential design strategy of BO treats f as a random function at first and places a prior over it. After gathering the tested data from the function evaluations, the posterior distribution over f is approximated by the updated prior. In turn, the observation of posterior distribution is used for the construction of an acquisition function that determines the next query point (combination).

- Activation function of visible layers in step 1: Affine
- Activation function of hidden layers in step 1: Sigmoid
- Hidden activation function in steps 2 and 3: ReLU
- Output activation function in steps 2 and 3: Softmax
- Loss function: Cross entropy
- Optimization algorithm: RMSProp and momentum
- Epochs: 50

- Parameter ranges:** Next query combination, e.g.:
1. Batch size: [8, 32] → (14)
 2. Learning rate: [$10^{-3}, 10^{-4}$] → (0.0005)
 3. Momentum rate: [0.1, 0.99] → (0.87)
 4. Dropout rate: [0.1, 0.5] → (0.3)
 5. Unit # of hidden layer 1: [800, 2000] → (1730)
 6. Unit # of hidden layer 2: [300, 700] → (600)
 7. Unit # of hidden layer 3: [20, 200] → (150)

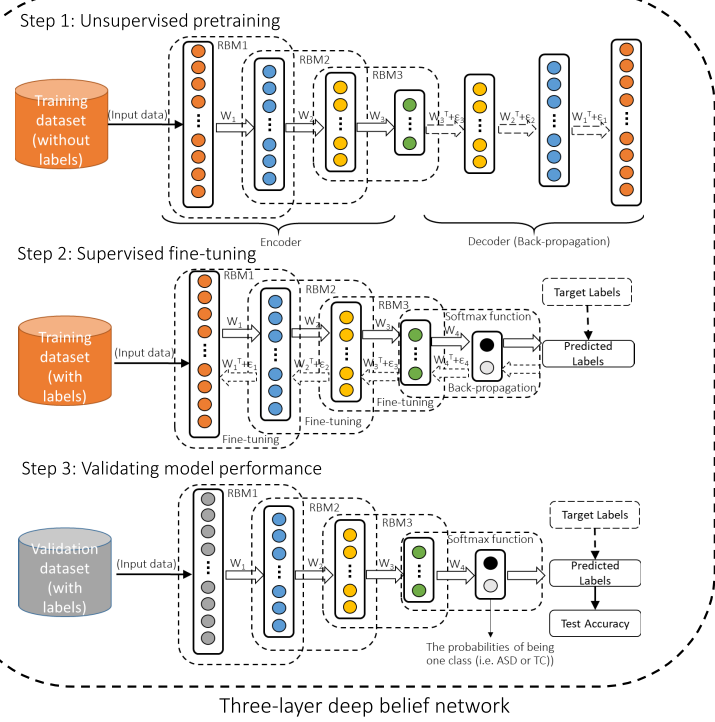
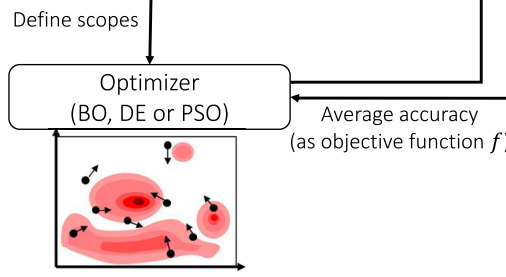


Fig. 5. Three-layer DBN classifier with automatic hyperparameter tuning of optimizer based on BO, DE, or PSO.

IV. EXPERIMENTS

For the evaluation of the efficiency and effectiveness of our model, all fMRI data sets from ABIDE are used to calculate the evaluation matrices (e.g., accuracy, sensitivity, specificity, ROC curve, and AUC) by tenfold CV. Seven state-of-the-art models are compared with the proposed model for the performance comparison. Then, differential evolution (DE) [54], [55] and particle swarm optimization (PSO) [56], [57] are applied as the global optimizers to compare with BO for the performance evaluation of hyperparameter tuning. We conduct a leave-one-site-out test to validate the applicability and generalization of the proposed model to the data from a new different site. The proposed model is leveraged to first identify three possible subtypes within ASD using data augmentation and the oversampling technique. We further conduct an analysis of the effects of confounding factors (e.g., age and gender) on classification accuracy. Finally, the predicted autistic neural patterns are manually validated based on the results reported in previous literatures.

A. ABIDE Data Set and Data Processing

The Autism Brain Imaging Data Exchange I (ABIDE) [14] database is a multisite open-access consortium collected from 17 different international brain imaging laboratories. In this study, we include all valid rs-fMRI data sets from 505 ASD patients and 530 TCs along with their key phenotypical information including age, subject gender, handedness, and full scale IQ. There is no consensus on the best way to preprocess the rs-fMRI data. To strengthen the data-sharing

effort in a better way, the Preprocessed Connectomes Project (<http://preprocessed-connectomes-project.org/abide/>) publicly releases the preprocessed version of ABIDE by five different teams using their preferred preprocessing strategies [53]. We select the data preprocessed through the Configurable Pipeline for the Analysis of Connectomes (C-PAC). This pipeline includes the slice time correction, motion realignment, global mean intensity normalization, nuisance variable regression, bandpass filtering (0.01–0.1 Hz), and functional image transformation. The nuisance variable regression is modeled with 24 motion parameters, five principal components of CompCor [58], and low-frequency drifts of the linear and quadratic trends to clean the confounding variations from the fMRI signal. The statistical derivatives are normalized to the MNI152 template space (3-mm isotropic) and spatially smoothed with a 6-mm Gaussian kernel of full width at half maximum (FWHM). The mean time series for each subject is extracted by the seed voxel signals in each nonoverlapping ROIs. There are seven ROI atlases providing different solutions to extract the mean time series of the functional data. Among these seven sets of ROIs, we use only the Craddock 200 (CC200) functional parcellation atlas for extraction in this work [59]. This data-driven parcellation atlas leverages the two-stage spatially functional procedure to partition the individual-level connectivity graphs into 200 regions by normalized cut spectral clustering.

B. Tenfold Cross Validation and Leave-One-Site-Out Test

We implement tenfold CV to investigate the performance of the proposed model. For each fold, the whole ABIDE

TABLE I

PERFORMANCE COMPARISON BETWEEN OUR MODEL AND OTHER PREVIOUS STUDIES BASED ON THE ABIDE DATABASE

Model	Classifier	Validation	sample #	Accuracy(STD)
Ours	DBN	10-fold CV	1035	0.764 (0.022)
Heinsfeld <i>et al.</i> [39]	DNN	10-fold CV	1035	0.700 (N.A.)
Dvornek <i>et al.</i> [40]	LSTM	10-fold CV	1035	0.685 (0.055)
Plitt <i>et al.</i> [19]	L-SVMs	10-fold CV	178	0.697 (0.027)
Chen <i>et al.</i> [20]	RFE-SVM	Train/Val	252	0.660 (N.A.)
Abraham <i>et al.</i> [28]	ℓ_2 -SVC	10-fold CV	871	0.669 (0.027)
Nielsen <i>et al.</i> [24]	LOO linear	LOOCV	964	0.600 (N.A.)
Ghiassian <i>et al.</i> [60]	RBF-SVM	Train/Val	1035	0.592 (N.A.)

database is split into training/validation/testing sets with a proportion of 8:1:1. The average elapsed time of training with the whole ABIDE database is about 96 s using one Intel Core CPU i7-8700K at 3.70 GHz and one NVIDIA GeForce RTX 2080 Ti GPU. Since the training time is shortened by feature reduction, sufficient numbers of iterations are allowed to find a better network parameter configuration for higher classification accuracy. For sufficient exploration in each fold CV, here, we limit the number of optimization iterations to 300 function evaluations (ten generations for DE and PSO with a population size of 30), where one function evaluation invokes one full training and evaluation of the DBN model. As we only focus on the ABIDE database in this work, the proposed DBN model is compared only with the other previous studies, whose results are also based on the ABIDE database. As shown in Table I, the four previous studies that do not use the whole ABIDE database tend to perform the ASD identification based on their specific sophisticated sampling criteria, which limits the generalizability of such methods. Arbabshirani *et al.* [28] demonstrated that the main bottleneck of this field is yet the limited sample size, and the high classification accuracy could degrade significantly when the sample data include over 100 participants. Therefore, the studies not using the whole ABIDE database could be more likely to suffer from overfitting based on the sophisticated sampling criteria. The main goal of our model is to achieve reliable diagnostic classification on large-scale aggregated data sets by extracting the reproducible autistic connectivity patterns. It is more desirable to put more focus on the studies based on the whole ABIDE database. As we can see, two DL-based models [39], [40] outperform all compared ML-based models [11], [19], [20], [24], [60] by using the DNN and the long short-term memory (LSTM) network, respectively. Besides the tenfold CV, the leave-one-out cross validation (LOOCV) and single training/validation set (Train/Val) are also used for validation. Our DBN model achieves a mean classification accuracy of 0.764 ± 0.022 (sensitivity: 0.778 and specificity: 0.750) in terms of tenfold CV, which has been the highest accuracy achieved so far. In this work, the sensitivity tells us what percentage of ASD subjects are correctly identified, while the specificity indicates that the percentage of people without ASD is correctly identified.

Since hyperparameter tuning in this case can be considered as a single objective optimization problem, DE and PSO are the population-based metaheuristic algorithms, which can

achieve outstanding optimization performance when sufficient numbers of iterations are allowed. Therefore, DE and PSO are used to compare with BO for performance evaluation. Fig. 6 shows the performance of our model with three different optimizers, as the number of generations increases. Random search is also used for the performance comparison as a baseline. For the proper division of the ABIDE data into training/validation/testing sets, we perform two ways of stratified random sampling by maintaining the balance of label distribution [shown in Fig. 6(a)] and each site frequency [shown in Fig. (b)], respectively. The effect of the stratified random sampling based on each site frequency is slightly worse than that of the stratified random sampling based on label distribution. As shown in Fig. 6(b), the BO-based optimizer achieves the highest accuracy of 0.762, while the other three optimizers show different levels of performance degradation, which could be attributed to the sample number imbalance between each of the sites. Within two generations, all compared optimizers tend to show slower convergence. Consequently, we adopt the label distribution-based stratified random sampling for data splitting in the following simulation experiments. In Fig. 6(a), within two generations, the BO-based optimizer shows faster convergence, while the other two optimizers perform like a random search. Then, the BO-based optimizer gets stuck on local optima, while the other two optimizers manage to find a near-optimal global solution. Finally, the DE-based optimizer obtains the highest accuracy of 0.764, which is comparable with the PSO-based optimizer's accuracy 0.763. In addition, the accuracy of the BO-based optimizer is 0.756. Considering the expensive computational cost of DBN training, BO tends to obtain better tradeoff of accuracy and efficiency.

The evaluation of most previous studies is based on one time CV schema. However, the effect of random sample divisions in CV should be considered. To reduce such a bias, ten times of tenfold CV are conducted in our model using the BO-based optimizer (see Table II). Only one generation (i.e., 30 iterations) is allowed for each fold CV in order to evaluate its feasibility and practicability within finite time. RF, SVM, and CNN (convolutional neural network [61], [62]) models are used for performance comparison under the same feature-selection framework. The architecture and setting of the CNN are shown in Fig. 7. For fair test, the parameters of RF and SVM are optimized from all potential parameter combinations by GridSearchCV, a grid-search module from scikit-learn [36]. As the best model reported to date using the whole ABIDE database, Heinsfeld's framework with different classifiers is also used for comparison. The results derived from their article [39] are based on one time tenfold CV. For a comprehensive assessment of our model, the results of three scenarios are analyzed, i.e., the mean-case, best case, and worst case scenarios. As we can see in Table II, random sample divisions do cause a certain impact on accuracy ranging from 3.3% to 1.3% in our work with different classifiers. Under the proposed feature-selection framework, RF and SVM achieve the mean accuracies of 0.656 and 0.670, respectively, which are nearly 2% higher than those in Heinsfeld's work. Note that Heinsfeld's work employed the entire connectivity

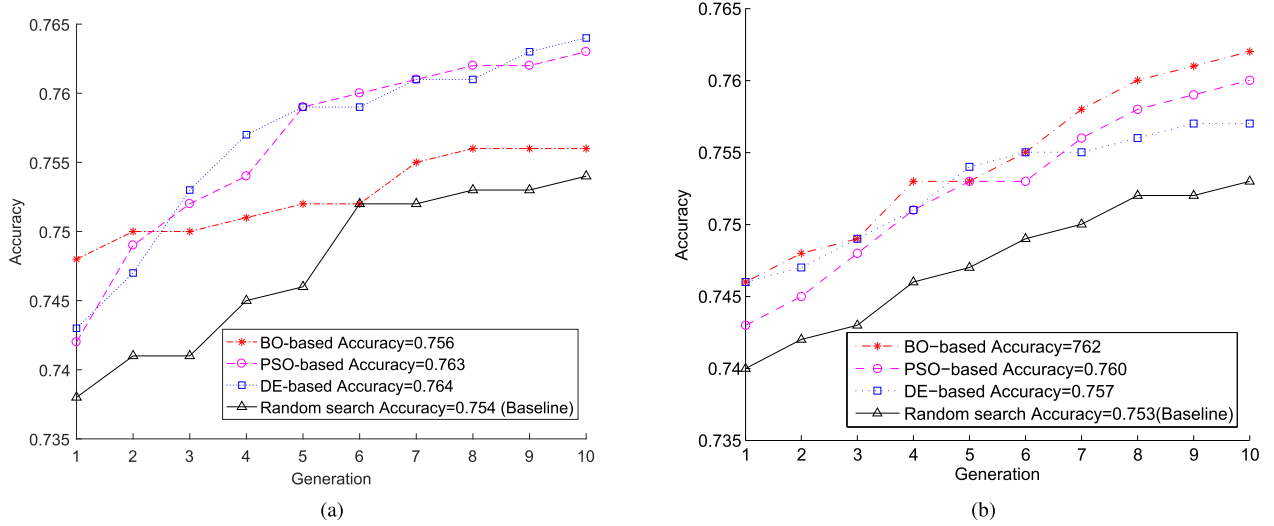


Fig. 6. Optimal convergence achieved by our model with three different optimizers as the generation number of hyperparameter tuning increases. (a) Stratified random sampling based on label distribution. (b) Stratified random sampling based on each site frequency.

TABLE II
PERFORMANCE COMPARISON BETWEEN OUR WORK AND HEINSFELD'S WORK BASED ON DIFFERENT CLASSIFIERS

Ten times 10-fold CV in our work under the same feature selection framework					One time 10-fold CV in Heinsfeld's work [39]				
Ours	Mean			Best	Worst	Classifier	Sensitivity	Specificity	Accuracy (STD)
Classifier	Sensitivity	Specificity	Accuracy (STD)	Accuracy (STD)	Accuracy (STD)	RF	0.69	0.58	0.63 (N.A.)
RF	0.734	0.580	0.656 (0.046)	0.665 (0.031)	0.650 (0.024)	SVM	0.68	0.62	0.65 (N.A.)
SVM	0.691	0.646	0.670 (0.047)	0.682 (0.041)	0.649 (0.057)	DNN	0.74	0.63	0.70 (N.A.)
DBN	0.762	0.731	0.745 (0.031)	0.751 (0.029)	0.738 (0.027)				
CNN	0.745	0.726	0.733 (0.046)	0.736 (0.041)	0.718 (0.052)				

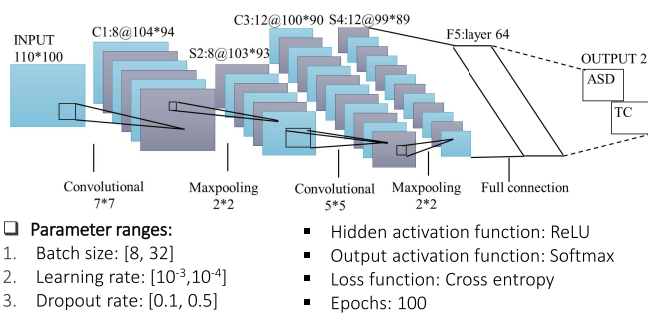


Fig. 7. Architecture and setting of the CNN are designed by manual tuning. Batch size, learning rate, and dropout rate are optimized by the BO-based optimizer.

features, whereas the proposed model uses only 16.52% of them. This result well demonstrates the effectiveness of our model. As expected, the DL-based classifiers outperform the traditional ML-based classifiers. The DBN achieves the best performance with the mean accuracy of 0.745 ± 0.031 . The translation invariance property of the CNN may be more suitable to resolve the image classification problems, instead of such graph-structured feature data. This result demonstrates the successful application of the DBN to the complex brain imaging data, showing high potential of neural networks for learning and detecting the underlying relationships between

TABLE III
PERFORMANCE COMPARISON FOR USING GBFS, RP-DFS, AND BO IN THE DBN MODEL BY TEN TIMES TENFOLD CV

	Mean accuracy	Sensitivity	Specificity
DBN with GBFS	0.716 (0.035)	0.750	0.676
DBN with GBFS,RP-DFS	0.725 (0.037)	0.740	0.710
DBN with GBFS,RP-DFS,BO	0.745 (0.031)	0.762	0.731

the extracted features acquired from the neuroimaging data and the psychological representations.

The contributions of the three proposed methods are also evaluated in Table III, i.e., GBFS, RP-DFS, and the automatic hyperparameter tuning of BO. Given the reliable performance of the GBFS method, three representative methods are used for performance comparison, i.e., the RF wrapper method [63], the t-test filter method [64], and the chi-squared statistic filter method [65]. As shown in Table IV, the proposed GBFS method achieves the reliable overall performance with the highest mean accuracy and specificity. The other three compared methods can obtain high sensitivities. Specifically, the RF wrapper method obtains the highest sensitivity of 0.806. However, they all fail to manage a tradeoff between sensitivity and specificity, which likely fluctuates their mean accuracies with relatively high STDs. The comparison

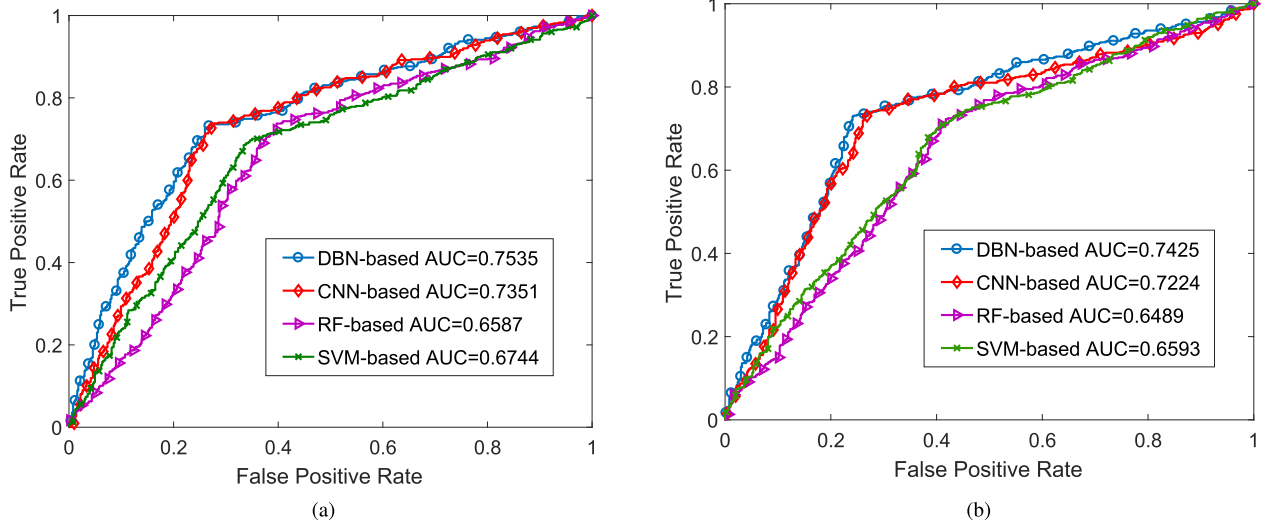


Fig. 8. Classification performance of the best case and worst case scenarios for the four classifiers evaluated by the ROC curve and AUC in tenfold CV. (a) Best-case scenario for the four classifiers in our work. (b) Worst case scenario for the four classifiers in our work.

TABLE IV
PERFORMANCE COMPARISON BETWEEN GBFS AND THE
REPRESENTATIVE FEATURE-SELECTION METHODS
BY TEN TIMES TENFOLD CV

Method	Class	Mean accuracy	Sensitivity	Specificity
GBFS	Filter	0.745 (0.031)	0.762	0.731
RF	Wrapper	0.734 (0.042)	0.806	0.641
T-test	Filter	0.693 (0.058)	0.764	0.598
Chi-squared	Filter	0.687 (0.069)	0.768	0.606

results demonstrate the superiority of the proposed method for FC feature selection.

Since the primary goal of this work is the intelligent auxiliary diagnosis for individuals with ASD, the sensitivity is more preferable to the specificity. It means that the missed diagnosis could bring more severe consequences than the misdiagnosis does. ROC and AUC are widely used to evaluate the performance of the binary classification problems by calculating the true-positive rate (sensitivity) and false-positive rate (1-specificity) by changing the thresholds. The ROC curve and the AUC value are used to observe the performance of our model for the best case and worst case scenarios by tenfold CV (see Fig. 8). As a result, the DBN achieves the highest AUC values of 0.7535 and 0.7425 in the best case and worst case scenarios, respectively. The DBN and CNN can obtain a good true-positive rate, while maintaining a relatively low false-positive rate. Table II also demonstrates that the sensitivities of DBN and CNN are higher than their specificities. Moreover, to investigate the potential of the deeper learning network in the DBN, we conduct a contrast experiment by gradually increasing the hidden layers of the architecture from three to five. Based on the result of Table V, the three-layer architecture is thereby adopted in the DBN model. The filter factor α and the number of nearest neighbor ROIs K are two key parameters for the proposed GBFS method. The selection of α and K is determined based on the experimental result

TABLE V
PERFORMANCE COMPARISON FOR DEEPER LEARNING NETWORK
IN DBN BY TEN TIMES TENFOLD CV

Layers	3	4	5
Average accuracy	0.745 (0.031)	0.737 (0.025)	0.727 (0.026)

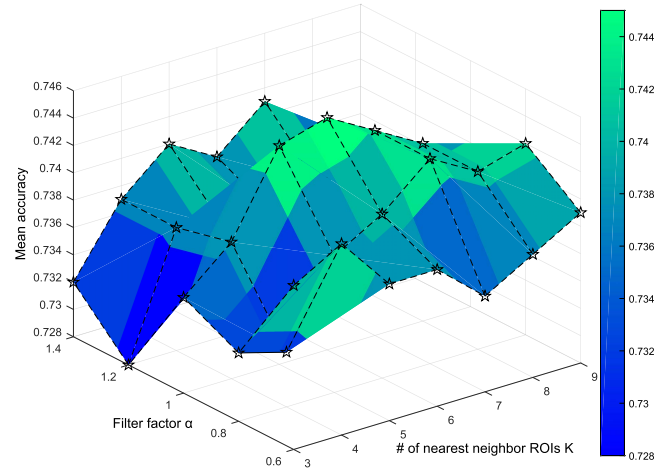


Fig. 9. Parameter tuning of α and K via tenfold CV. The lighter the color you observe, the higher the mean accuracy of the area it represents.

of tenfold CV, as shown in Fig. 9. As we can see, the best performance is achieved with the combination of $\alpha = 1$ and $K = 6$. Therefore, the values of α and K are empirically set to 1 and 6, respectively.

Since ABIDE is the repository aggregated across 17 international sites without prior coordination, the proposed model should be reliable enough against the effects brought by different experimental settings and participants. The leave-one-site-out test is used to evaluate the applicability and generalization of the proposed model to a new different site.

TABLE VI
LEAVE-ONE-SITE-OUT TEST

Site	Vendor	FD	# of ASD	# of TC	Accuracy
KKI	Philips	0.17	22 (8-13)	33 (8-13)	0.792
LEUVEN	Philips	0.09	29 (12-32)	35 (12-32)	0.810
SBL	Philips	0.16	15 (22-64)	15 (20-41)	0.667
TRINITY	Philips	0.11	24 (12-26)	25 (12-26)	0.766
NYU	Siemens	0.07	79 (7-39)	105 (7-32)	0.743
OHSU	Siemens	0.10	13 (8-15)	15 (8-12)	0.731
OLIN	Siemens	0.18	20 (11-24)	15 (10-23)	0.765
PITT	Siemens	0.15	30 (9-35)	27 (9-33)	0.786
UCLA	Siemens	0.19	62 (8-18)	47 (9-18)	0.786
MAX_MUN	Siemens	0.13	24 (7-58)	33 (7-48)	0.673
CMU	Siemens	0.29	14 (19-39)	13 (20-40)	0.889
USM	Siemens	0.14	58 (11-50)	43 (9-39)	0.859
CALTECH	Siemens	0.07	19 (17-45)	19 (17-56)	0.811
YALE	Siemens	0.11	28 (7-18)	28 (8-18)	0.839
SDSU	GE	0.09	14 (12-17)	22 (9-17)	0.806
STANFORD	GE	0.11	20 (8-13)	20 (8-12)	0.795
UM	GE	0.14	68 (8-19)	77 (8-29)	0.771
Mean	N.A.	0.14	31.7	33.6	0.782

As for the leave-one-site-out test, the data sets from one site are used to test the classification accuracy, while the remaining data sets from other sites are split into training/validation sets in a proportion of 8:2. MRI vendors, mean framework displacement (FD), and phenotypic information are selected as three representative factors. Age ranges are correspondingly marked in brackets. Mean FD is a measure of the subject head motion to compare the change between the current and previous volumes. The lower value of the mean FD indicates the less subject head motion. As we can see in Table VI, the proposed model achieves the mean accuracy of 0.782. Four sites show significantly lower accuracies than the mean: SBL, NYU, OHSU, and MAX_MUN. Note that the accuracies of SBL, OHSU, and MAX_MUN are also significantly lower the mean in Heinsfeld's work [39]. This means that these sites might hold site-specific variability and heterogeneity that are being absent in other sites. The result suggests that there is no significant effect of MRI vendor, mean FD, and phenotypic information on the classification performance. It could be concluded that the proposed model holds a high reliability against the uncertainties from the new sites.

C. Identification of Possible Subtypes Within ASD

As a range of mental disorders, ASD can be further diagnosed as autism, Asperger syndrome, pervasive developmental disorder not otherwise specified (PDD-NOS), and so on, based on the domains of impairment in the ASD (see Table VII) [2]. The subtle changes in their clinical presentations are challenging to be detected and distinguished by the symptom-based diagnostic criteria, and that obstructs more precise therapeutic decision-making for individuals with ASD. To the best of our knowledge, no computational models have been proposed to identify possible subtypes within the ASD using the

TABLE VII
DOMAINS OF IMPAIRMENT IN ASD AND SAMPLE NUMBERS OF ASD SUBTYPES IN ABIDE

	Autism	Asperger	PDD-NOS
social communication	required	required	required
language	required	normal	variable
repetitive behaviors	required	required	variable
Sample # in ABIDE	323	87	35

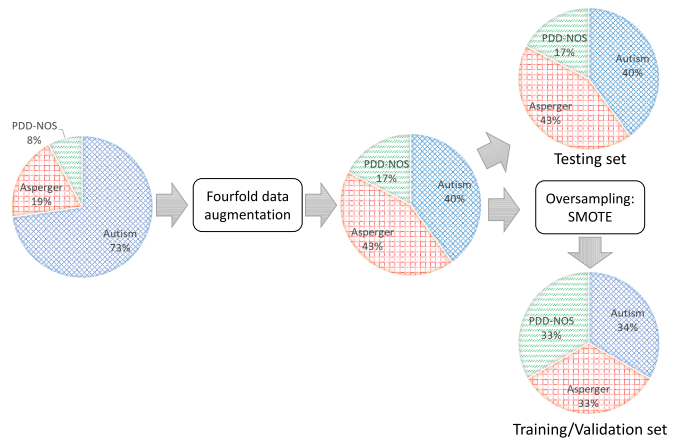


Fig. 10. Data augmentation and SMOTE are used for balancing the data sets.

fMRI data. In this study, we try to leverage the proposed model to address this issue as a multiclass classification problem. Table VII shows that the ABIDE database is imbalanced for consisting of 323 autism samples, 87 Asperger samples, and 35 PDD-NOS samples, with a ratio of 9.2:2.5:1.

To balance the data set before training, data augmentation and oversampling are used (see Fig. 10). First, we randomly crop the raw input time course to the same sequence length for each sample of Asperger and PDD-NOS. Considering the length of the shortest time series, we make such a fourfold augmentation to yield more sample data for training and testing. However, PDD-NOS samples still make up a small percentage of 17% of the augmented data sets, where the amount of Asperger samples is comparable with the autism samples. It means that more PDD-NOS samples are required for training the model. The synthetic minority oversampling technique (SMOTE) [66] is introduced to synthesize the new minority instances (i.e., PDD-NOS samples) between a pair of one minority instance and one of its K nearest neighbors. To be fair, SMOTE is not used for the test set, preventing a high rate of false-positive results. Finally, the proposed model is implemented on the augmented data sets likewise. To evaluate better such imbalanced data, F1-measure is used as a measure metrics for each ASD subtype as follows:

$$\left\{ \begin{array}{l} \text{F1-measure} = \frac{2 \times \text{precision} \times \text{recall}}{(\text{precision} + \text{recall})} \\ \text{precision} = \frac{\text{True positive}}{\text{True positive} + \text{False positive}} \\ \text{recall} = \frac{\text{True positive}}{\text{True positive} + \text{False negative}} \end{array} \right. \quad (6)$$

TABLE VIII
COMPARISON RESULTS FOR IDENTIFICATION OF ASD SUBTYPES BY TEN TIMES TENFOLD CV

Classifier	Autism	Asperger	PDD-NOS	Total
	F1-measure			Macro-average accuracy
DBN	0.940	0.902	0.603	0.838
CNN	0.922	0.915	0.547	0.828
RF	0.880	0.806	0.362	0.761
SVM	0.933	0.887	0.471	0.802

Macro-average accuracy is also used to evaluate globally the performance by weighting toward the minority class, i.e., the PDD-NOS samples. As shown in Table VIII, all compared classifiers obtain the reliable performance in the samples of autism and Asperger by the same feature selection of GBFS. The DBN classifier achieves the highest macro-average accuracy of 0.838. All classifiers in different extents show biased predictive capability that has a higher F1-measure over the majority classes but poorer F1-measure over the minority class. However, the DBN classifier shows moderate improvement in prediction performance on the PDD-NOS samples. By taking out the minority class, i.e., PDD-NOS, we also use the proposed model to identify autism and Asperger syndrome. In ten times tenfold CV, the proposed model achieves the satisfactory mean accuracy of 0.896 ± 0.030 with a high sensitivity of 0.885 and a high specificity of 0.907. It demonstrates that our model can make a reliable identification for autism and Asperger syndrome.

It also needs to note that there are some downsides to perform data augmentation and oversampling on the data sets. Since we make a fourfold augmentation to yield more sample data for training and testing, the extracted FC features are derived from the shorter mean time series of rs-fMRI data, i.e., a quarter of the original ones. The quality of the extracted feature could be affected to a certain extent. Furthermore, the oversampling technique can create the synthetic examples without considering the majority class (i.e., autism and Asperger syndrome in this study). It could lead to overfitting to the training data. To be sure, every approach has its own downsides. Nevertheless, using data augmentation and oversampling in our model is quite effective to increase the training samples and equilibrate the class weights by mitigating the issue of class imbalance. This work is expected to provide valuable insights into the identification of possible subtypes within ASD using the fMRI data.

D. Effects of Confounding Factors on Classification Accuracy

Some neuroscientific work may specify the recruitment strategies and participant instructions for particular research purposes. For example, in general, children with ASD should be diagnosed before 6 years old; otherwise, it would be too late for effective treatments. When testing the sample sets with a certain condition (e.g., age < 6), a reliable model should keep robustness and show no significant difference in accuracy based on the remaining samples as the training data. Therefore, it is necessary to evaluate the effects of confounding factors

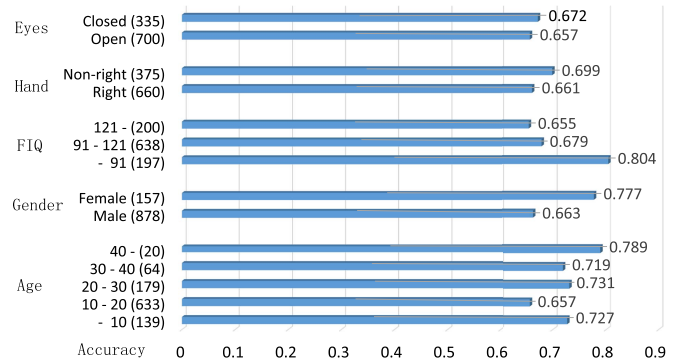


Fig. 11. Effects of eye status, handedness, FIQ, gender, and age are evaluated on prediction accuracy as confounding factors. The sample numbers are given in brackets.

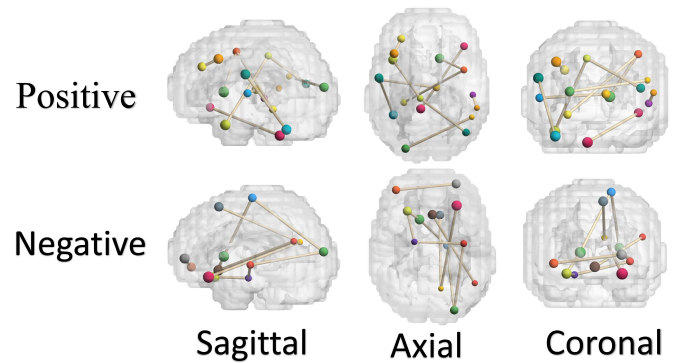


Fig. 12. Most positively/negatively correlated predicted connections with the highest/lowest scores.

on classification accuracy. As shown in Fig. 11, basically, there are no significant differences observed between accuracy and the confounding factors including eye status, handedness, FIQ scores, gender, and age. The imbalanced data sets have a negative effect on prediction accuracy. It should be noted that the accuracy of the low FIQ group (< 91) is 14.9% higher than that of the high FIQ group (> 121) based on the balanced sample data. This result suggests that intellectual disability could be a good diagnostic feature for the ASD subjects.

E. Model Interpretation: Neural Patterns in the Autistic Brain

Based on the connectivity matrices refined by RP-DFS, the correlations between two ROIs are represented by the accumulated scores from all potential paths. Given the assumptions of such correlation patterns, those connections with high accumulated scores could be highly connected (positively correlated). Otherwise, the connections with low accumulated scores tend to be underconnected (negatively correlated). To derive the reproducible autistic neural patterns, the top-10 ranked remarkable connections are selected based on their mean scores from the ASD group (see Fig. 12). Then, their ROIs are manually validated according to the results reported in the previous literatures. Table IX demonstrates the manual validation of those involved ROIs that have been confirmed to have associations with ASD by the Digital Object Identifiers (DOIs). The ROI numbers of CC200 atlas are given

TABLE IX
MANUAL VALIDATION FOR THOSE INVOLVED ROIS IN PREDICTED AUTISTIC CONNECTIONS BASED ON PREVIOUS LITERATURES

ROI	DOI	ROI	DOI	Score
Top-10 positively correlated predicted connections in the autistic brain				
Left Fusiform Gyrus (122)	10.1001/archgenpsychiatry.2010.31	Right Precentral Gyrus (115)	10.1097/01.wnr.0000233087.15710.87	1.8842 (1)
Left Superior Temporal Gyrus (146)	10.1016/j.pscychresns.2005.12.009	Right Thalamus (18)	10.1016/j.brainres.2009.12.081	1.6430 (2)
Right Middle Temporal Gyrus (69)	10.1017/S1355617708081216	Right Middle Temporal Gyrus (107)	10.1017/S1355617708081216	1.4668 (3)
Left Middle Cingulate Cortex (76)	unconfirmed	Right Middle Temporal Gyrus (85)	10.1017/S1355617708081216	1.4565 (4)
Right Caudate Nucleus (135)	10.1186/s11689-015-9107-8	Right Precentral Gyrus (115)	10.1007/s10803-011-1221-1	1.3202 (5)
Right Middle Temporal Gyrus (14)	10.1017/S1355617708081216	Left Middle Occipital Gyrus (131)	unconfirmed	1.3064 (6)
Left Middle Frontal Gyrus (125)	unconfirmed	Left Middle Frontal Gyrus (61)	unconfirmed	1.3018 (7)
Left Postcentral Gyrus (88)	10.1016/j.biopsych.2015.10.020	Left Cerebellum (36)	unconfirmed	1.2491 (8)
Right Inferior Frontal Gyrus (53)	10.1016/j.neuroimage.2004.12.022	Left Cerebellum (52)	unconfirmed	1.2473 (9)
Left Middle Cingulate Cortex (76)	unconfirmed	Left Temporal Pole (78)	10.1016/j.biopsych.2012.12.013	1.2431 (10)
Top-10 negatively correlated predicted connections in the autistic brain				
Left Precentral Gyrus (90)	10.1136/jnnp.2010.239111	Left Middle Occipital Gyrus (131)	unconfirmed	-0.2706 (1)
Right Frontal Orbital Cortex (71)	unconfirmed	Right Parahippocampal Gyrus (155)	10.1016/j.neuroimage.2009.04.069	-0.2696 (2)
Right Frontal Orbital Cortex (71)	unconfirmed	Right Caudate Nucleus (135)	10.1186/s11689-015-9107-8	-0.2480 (3)
Left Superior Frontal Gyrus (173)	10.1016/j.brainresbull.2010.12.002	Left Precuneous Cortex (19)	unconfirmed	-0.2479 (4)
Right Caudate Nucleus (135)	10.1186/s11689-015-9107-8	Left Precentral Gyrus (90)	10.1136/jnnp.2010.239111	-0.2447 (5)
Left Putamen (4)	10.1007/s12264-017-0118-1	Right Parahippocampal Gyrus (155)	10.1016/j.neuroimage.2009.04.069	-0.2436 (6)
Left Middle Temporal Gyrus (2)	10.1016/j.expneurol.2003.09.010	Right Subcallosal Cortex	unconfirmed	-0.2423 (7)
Right Frontal Pole (113)	10.1016/j.biopsych.2013.06.018	Left Frontal Pole (183)	10.1016/j.neuroimage.2004.02.029	-0.2421 (8)
Left Precuneous Cortex (19)	unconfirmed	Left Frontal Orbital Cortex (57)	unconfirmed	-0.2417 (9)
Left Middle Occipital Gyrus (131)	unconfirmed	Left Putamen (4)	10.1007/s12264-017-0118-1	-0.2385 (10)

in brackets. The result shows that 65% (13/20) and 60% (12/20) of the involved ROIs are confirmed to have highly connected function and underconnected function in the autistic brain, respectively. Furthermore, these experimental data are consistent with the findings from the previous literatures. For examples, in adults with ASD, a specific focal increase in cortical thickness is found at the left fusiform gyrus (122) [67]. It could result in the associated impairments in face processing for the ASD subjects. In this work, the left fusiform gyrus (122) is predicted to have a strong positive correlation (first in the prediction list) with the right precentral gyrus (115) in the autistic brain. Moreover, the area of the reduced gray matter volumes in autistic children is found in the left superior frontal gyrus (173) by the analysis of voxel-based morphometry [68]. In this work, the left superior frontal gyrus (173) is predicted to have a strong negative correlation (fourth in the prediction list) with the left precuneous cortex (19) in the autistic brain. These predicted autistic neural patterns are anticipated to serve as reproducible biomarkers, offering insights into the pathophysiological mechanism of the ASD.

V. CONCLUSION

We presented a novel graph-based computational model for the identification of the ASD using the rs-fMRI data. A GBFS method was proposed to highlight the remarkable connections by both external and internal measures. To take advantage of the topological information implied in the graph, RP-DFS was proposed to refine further the remarkable connectivity matrices. Finally, a three-layer DBN model with the automatic hyperparameter-tuning technique was applied for classification. Compared with other state-of-the-art methods,

our model achieved the highest mean accuracy of 0.764 ± 0.022 . The reliable performance was fully demonstrated by the comprehensive experiments. This work also provides an insight into the identification of possible subtypes within ASD. By a statistical analysis, the interpretability of our model enabled to uncover the correlation patterns in the autistic brain. This article is anticipated to serve as a candidate tool for identifying the ASD subjects using the rs-fMRI data. We expect that the proposed model could offer insights into the computer-aided diagnosis of complex psychological disorders using neural network models.

For future work, it would be interesting to develop a multitask learning classification framework to capture the site-shared and site-specific feature patterns from the multisite imaging data. The merits of multimodal data fusion [69] can be used to improve the spatiotemporal resolution of characterization of the brain state by combining the rs-fMRI and structural MRI (sMRI) data.

REFERENCES

- [1] A. V. Buescher, Z. Cidav, M. Knapp, and D. S. Mandell, "Costs of autism spectrum disorders in the United Kingdom and the United States," *JAMA Pediatrics*, vol. 168, no. 8, pp. 721–728, 2014.
- [2] D. H. Geschwind, "Advances in autism," *Annu. Rev. Med.*, vol. 60, pp. 367–380, Feb. 2009.
- [3] E.-M. Rødgaard, K. Jensen, J.-N. Vergnes, I. Soulières, and L. Mottron, "Temporal changes in effect sizes of studies comparing individuals with and without autism: A meta-analysis," *JAMA Psychiatry*, vol. 76, no. 11, p. 1124, Nov. 2019.
- [4] S. A. Huettel *et al.*, *Functional Magnetic Resonance Imaging*, vol. 1. Sunderland, MA, USA: Sinauer Associates, 2004.
- [5] G. Chen *et al.*, "Classification of alzheimer disease, mild cognitive impairment, and normal cognitive status with large-scale network analysis based on resting-state functional MR imaging," *Radiology*, vol. 259, no. 1, pp. 213–221, Apr. 2011.

- [6] Z. Yu-Feng *et al.*, "Altered baseline brain activity in children with ADHD revealed by resting-state functional MRI," *Brain Develop.*, vol. 29, no. 2, pp. 83–91, Mar. 2007.
- [7] V. L. Cherkassky, R. K. Kana, T. A. Keller, and M. A. Just, "Functional connectivity in a baseline resting-state network in autism," *NeuroReport*, vol. 17, no. 16, pp. 1687–1690, Nov. 2006.
- [8] J. S. Anderson *et al.*, "Functional connectivity magnetic resonance imaging classification of autism," *Brain*, vol. 134, no. 12, pp. 3742–3754, Dec. 2011.
- [9] M. Greicius, "Resting-state functional connectivity in neuropsychiatric disorders," *Current Opinion Neurol.*, vol. 24, no. 4, pp. 424–430, Aug. 2008.
- [10] F. X. Castellanos, A. Di Martino, R. C. Craddock, A. D. Mehta, and M. P. Milham, "Clinical applications of the functional connectome," *NeuroImage*, vol. 80, pp. 527–540, Oct. 2013.
- [11] A. Abraham *et al.*, "Deriving reproducible biomarkers from multi-site resting-state data: An autism-based example," *NeuroImage*, vol. 147, pp. 736–745, Feb. 2017.
- [12] D. Nie, L. Wang, Y. Gao, J. Lian, and D. Shen, "STRAINet: Spatially varying stochastic residual Adversarial networks for MRI pelvic organ segmentation," *IEEE Trans. Neural Netw. Learn. Syst.*, vol. 30, no. 5, pp. 1552–1564, May 2019.
- [13] G. Hinton, "Deep belief networks," *Scholarpedia*, vol. 4, no. 5, p. 5947, 2009.
- [14] A. Di Martino *et al.*, "The autism brain imaging data exchange: Towards a large-scale evaluation of the intrinsic brain architecture in autism," *Mol. Psychiatry*, vol. 19, no. 6, p. 659, 2014.
- [15] K. S. Kassam, A. R. Markey, V. L. Cherkassky, G. Loewenstein, and M. A. Just, "Identifying emotions on the basis of neural activation," *PLoS ONE*, vol. 8, no. 6, Jun. 2013, Art. no. e66032.
- [16] A. J. Bauer and M. A. Just, "Monitoring the growth of the neural representations of new animal concepts," *Hum. Brain Mapping*, vol. 36, no. 8, pp. 3213–3226, Aug. 2015.
- [17] A. J. O'Toole, F. Jiang, H. Abdi, and J. V. Haxby, "Partially distributed representations of objects and faces in ventral temporal cortex," *J. Cognit. Neurosci.*, vol. 17, no. 4, pp. 580–590, Apr. 2005.
- [18] N. Yahata, K. Kasai, and M. Kawato, "Computational neuroscience approach to biomarkers and treatments for mental disorders," *Psychiatry Clin. Neurosci.*, vol. 71, no. 4, pp. 215–237, Apr. 2017.
- [19] M. Plitt, K. A. Barnes, and A. Martin, "Functional connectivity classification of autism identifies highly predictive brain features but falls short of biomarker standards," *NeuroImage, Clin.*, vol. 7, pp. 359–366, Jan. 2015.
- [20] C. P. Chen *et al.*, "Diagnostic classification of intrinsic functional connectivity highlights somatosensory, default mode, and visual regions in autism," *NeuroImage, Clin.*, vol. 8, pp. 238–245, Jan. 2015.
- [21] M. Mahmud, M. S. Kaiser, A. Hussain, and S. Vassanelli, "Applications of deep learning and reinforcement learning to biological data," *IEEE Trans. Neural Netw. Learn. Syst.*, vol. 29, no. 6, pp. 2063–2079, Jun. 2018.
- [22] F. Zhao, H. Zhang, I. Rekik, Z. An, and D. Shen, "Diagnosis of autism spectrum disorders using multi-level high-order functional networks derived from resting-state functional MRI," *Frontiers Hum. Neurosci.*, vol. 12, p. 184, May 2018.
- [23] M. Kachuee, S. Darabi, B. Moatamed, and M. Sarrafzadeh, "Dynamic feature acquisition using denoising autoencoders," *IEEE Trans. Neural Netw. Learn. Syst.*, vol. 30, no. 8, pp. 2252–2262, Aug. 2019.
- [24] J. A. Nielsen *et al.*, "Multisite functional connectivity MRI classification of autism: ABIDE results," *Frontiers Hum. Neurosci.*, vol. 7, p. 599, Sep. 2013.
- [25] Y. Du, Z. Fu, and V. D. Calhoun, "Classification and prediction of brain disorders using functional connectivity: Promising but challenging," *Frontiers Neurosci.*, vol. 12, p. 525, Aug. 2018.
- [26] A. Khazaee, A. Ebrahimzadeh, and A. Babajani-Feremi, "Identifying patients with Alzheimer's disease using resting-state fMRI and graph theory," *Clin. Neurophysiol.*, vol. 126, no. 11, pp. 2132–2141, Nov. 2015.
- [27] E. Challis, P. Hurley, L. Serra, M. Bozzali, S. Oliver, and M. Cercignani, "Gaussian process classification of Alzheimer's disease and mild cognitive impairment from resting-state fMRI," *NeuroImage*, vol. 112, pp. 232–243, May 2015.
- [28] M. R. Arbabsirani, S. Plis, J. Sui, and V. D. Calhoun, "Single subject prediction of brain disorders in neuroimaging: Promises and pitfalls," *NeuroImage*, vol. 145, pp. 137–165, Jan. 2017.
- [29] Y. Du *et al.*, "A group ICA based framework for evaluating resting fMRI markers when disease categories are unclear: Application to schizophrenia, bipolar, and schizoaffective disorders," *NeuroImage*, vol. 122, pp. 272–280, Nov. 2015.
- [30] J. Yang and V. Honavar, "Feature subset selection using a genetic algorithm," in *Feature Extraction, Construction Selection*. Boston, MA, USA: Springer, 1998, pp. 117–136.
- [31] T. Iidaka, "Resting state functional magnetic resonance imaging and neural network classified autism and control," *Cortex*, vol. 63, pp. 55–67, Feb. 2015.
- [32] V. Fonti and E. Belitsir, "Feature selection using lasso," *VU Amsterdam Res. Paper Bus. Anal.*, vol. 30, pp. 1–25, Mar. 2017.
- [33] J. Wang *et al.*, "Multi-task diagnosis for autism spectrum disorders using multi-modality features: A multi-center study," *Hum. Brain Mapping*, vol. 38, no. 6, pp. 3081–3097, Jun. 2017.
- [34] D. Zhang and D. Shen, "Multi-modal multi-task learning for joint prediction of multiple regression and classification variables in Alzheimer's disease," *NeuroImage*, vol. 59, no. 2, pp. 895–907, Jan. 2012.
- [35] H. Wang *et al.*, "Identifying disease sensitive and quantitative trait-relevant biomarkers from multidimensional heterogeneous imaging genetics data via sparse multimodal multitask learning," *Bioinformatics*, vol. 28, no. 12, pp. i127–i136, Jun. 2012.
- [36] F. Pedregosa *et al.*, "Scikit-learn: Machine learning in Python," *J. Mach. Learn. Res.*, vol. 12, pp. 2825–2830, Oct. 2011.
- [37] X. Pan and Y. Xu, "A novel and safe two-stage screening method for support vector machine," *IEEE Trans. Neural Netw. Learn. Syst.*, vol. 30, no. 8, pp. 2263–2274, Aug. 2019.
- [38] T. Zhai, F. Koriche, H. Wang, and Y. Gao, "Tracking sparse linear classifiers," *IEEE Trans. Neural Netw. Learn. Syst.*, vol. 30, no. 7, pp. 2079–2092, Jul. 2019.
- [39] A. S. Heinsfeld, A. R. Franco, R. C. Craddock, A. Buchweitz, and F. Meneguzzi, "Identification of autism spectrum disorder using deep learning and the ABIDE dataset," *NeuroImage, Clin.*, vol. 17, pp. 16–23, Jan. 2018.
- [40] N. C. Dvornek, P. Ventola, K. A. Pelphrey, and J. S. Duncan, "Identifying autism from resting-state fmri using long short-term memory networks," in *Proc. Int. Workshop Mach. Learn. Med. Imag.* Cham, Switzerland: Springer, 2017, pp. 362–370.
- [41] M. Kholas, K. Jamison, A. Kuceyeski, and M. R. Sabuncu, "3D convolutional neural networks for classification of functional connectomes," in *Deep Learning in Medical Image Analysis and Multimodal Learning for Clinical Decision Support*. Cham, Switzerland: Springer, 2018, pp. 137–145.
- [42] W. Liu, Z. Wang, X. Liu, N. Zeng, Y. Liu, and F. E. Alsaadi, "A survey of deep neural network architectures and their applications," *Neurocomputing*, vol. 234, pp. 11–26, Apr. 2017.
- [43] C. Zhang, P. Lim, A. K. Qin, and K. C. Tan, "Multiobjective deep belief networks ensemble for remaining useful life estimation in prognostics," *IEEE Trans. Neural Netw. Learn. Syst.*, vol. 28, no. 10, pp. 2306–2318, Oct. 2017.
- [44] M. Xia, J. Wang, and Y. He, "BrainNet viewer: A network visualization tool for human brain connectomics," *PLoS ONE*, vol. 8, no. 7, Jul. 2013, Art. no. e68910.
- [45] M. A. Just, T. A. Keller, V. L. Malave, R. K. Kana, and S. Varma, "Autism as a neural systems disorder: A theory of frontal-posterior underconnectivity," *Neurosci. Biobehav. Rev.*, vol. 36, no. 4, pp. 1292–1313, Apr. 2012.
- [46] Z.-A. Huang *et al.*, "PBHMDA: Path-based human microbiome-disease association prediction," *Frontiers Microbiol.*, vol. 8, p. 233, Feb. 2017.
- [47] W. Ba-alawi, O. Soufan, M. Essack, P. Kalnis, and V. B. Bajic, "DASPfind: New efficient method to predict drug-target interactions," *J. Cheminformatics*, vol. 8, no. 1, p. 15, Dec. 2016.
- [48] C. L. P. Chen and S. Feng, "Generative and discriminative fuzzy restricted Boltzmann machine learning for text and image classification," *IEEE Trans. Cybern.*, vol. 50, no. 5, pp. 2237–2248, May 2020.
- [49] C. Zhang, K. C. Tan, H. Li, and G. S. Hong, "A cost-sensitive deep belief network for imbalanced classification," *IEEE Trans. Neural Netw. Learn. Syst.*, vol. 30, no. 1, pp. 109–122, Jan. 2019.
- [50] F. Zou, L. Shen, Z. Jie, W. Zhang, and W. Liu, "A sufficient condition for convergences of adam and RMSProp," in *Proc. IEEE/CVF Conf. Comput. Vis. Pattern Recognit. (CVPR)*, Jun. 2019, pp. 11127–11135.

- [51] Y. Li and Y. Yuan, "Convergence analysis of two-layer neural networks with Relu activation," in *Proc. Adv. Neural Inf. Process. Syst.*, 2017, pp. 597–607.
- [52] J. Snoek, H. Larochelle, and R. P. Adams, "Practical Bayesian optimization of machine learning algorithms," in *Proc. Adv. Neural Inf. Process. Syst.*, 2012, pp. 2951–2959.
- [53] C. Cameron *et al.*, "The neuro bureau preprocessing initiative: Open sharing of preprocessed neuroimaging data and derivatives," *Frontiers Neuroinform.*, early access, Jan. 7, 2013, doi: 10.3389/conf.fniinf.2013.09.00041.
- [54] L. Tang, X. Wang, and Z. Dong, "Adaptive multiobjective differential evolution with reference axis vicinity mechanism," *IEEE Trans. Cybern.*, vol. 49, no. 9, pp. 3571–3585, Sep. 2019.
- [55] S. X. Zhang, S. Y. Zheng, and L. M. Zheng, "An efficient multiple variants coordination framework for differential evolution," *IEEE Trans. Cybern.*, vol. 47, no. 9, pp. 2780–2793, Sep. 2017.
- [56] L. Li, L. Chang, T. Gu, W. Sheng, and W. Wang, "On the norm of dominant difference for many-objective particle swarm optimization," *IEEE Trans. Cybern.*, early access, Aug. 19, 2019, doi: 10.1109/TCYB.2019.2922287.
- [57] Y.-F. Zhang and H.-D. Chiang, "A novel consensus-based particle swarm optimization-assisted trust-tech methodology for large-scale global optimization," *IEEE Trans. Cybern.*, vol. 47, no. 9, pp. 2717–2729, Sep. 2017.
- [58] Y. Behzadi, K. Restom, J. Liau, and T. T. Liu, "A component based noise correction method (CompCor) for BOLD and perfusion based fMRI," *NeuroImage*, vol. 37, no. 1, pp. 90–101, Aug. 2007.
- [59] R. C. Craddock, G. A. James, P. E. Holtzheimer, X. P. Hu, and H. S. Mayberg, "A whole brain fMRI atlas generated via spatially constrained spectral clustering," *Hum. Brain Mapping*, vol. 33, no. 8, pp. 1914–1928, Aug. 2012.
- [60] S. Ghassian, R. Greiner, P. Jin, and M. R. G. Brown, "Using functional or structural magnetic resonance images and personal characteristic data to identify ADHD and autism," *PLoS ONE*, vol. 11, no. 12, Dec. 2016, Art. no. e0166934.
- [61] M. Buda, A. Maki, and M. A. Mazurowski, "A systematic study of the class imbalance problem in convolutional neural networks," *Neural Netw.*, vol. 106, pp. 249–259, Oct. 2018.
- [62] S. Pereira, A. Pinto, V. Alves, and C. A. Silva, "Brain tumor segmentation using convolutional neural networks in MRI images," *IEEE Trans. Med. Imag.*, vol. 35, no. 5, pp. 1240–1251, May 2016.
- [63] P. Geurts, D. Ernst, and L. Wehenkel, "Extremely randomized trees," *Mach. Learn.*, vol. 63, no. 1, pp. 3–42, Apr. 2006.
- [64] R. Chaves *et al.*, "SVM-based computer-aided diagnosis of the Alzheimer's disease using t-test NMSE feature selection with feature correlation weighting," *Neurosci. Lett.*, vol. 461, no. 3, pp. 293–297, Sep. 2009.
- [65] H. G. Schulze, R. B. Foist, A. Ivanov, and R. F. B. Turner, "Chi-squared-based filters for high-fidelity signal-to-noise ratio enhancement of spectra," *Appl. Spectrosc.*, vol. 62, no. 8, pp. 847–853, Aug. 2008.
- [66] N. V. Chawla, K. W. Bowyer, L. O. Hall, and W. P. Kegelmeyer, "SMOTE: Synthetic minority over-sampling technique," *J. Artif. Intell. Res.*, vol. 16, pp. 321–357, Jun. 2002.
- [67] I. Dziobek, M. Bahnemann, A. Convit, and H. R. Hecker, "The role of the fusiform-amygdala system in the pathophysiology of autism," *Arch. Gen. Psychiatry*, vol. 67, no. 4, pp. 397–405, 2010.
- [68] P. Mengotti *et al.*, "Altered white matter integrity and development in children with autism: A combined voxel-based morphometry and diffusion imaging study," *Brain Res. Bull.*, vol. 84, no. 2, pp. 189–195, Feb. 2011.
- [69] O. Dekhil *et al.*, "A personalized autism diagnosis CAD system using a fusion of structural MRI and resting-state functional MRI data," *Frontiers Psychiatry*, vol. 10, p. 392, Jul. 2019.



Zhi-An Huang received the B.Eng. degree in software engineering from Shenzhen University, Shenzhen, China, in 2018. He is currently pursuing the Ph.D. degree with the Department of Computer Science, City University of Hong Kong, Hong Kong.

His research interests include artificial intelligence, machine learning, bioinformatics, and medical imaging analysis.



Xuean Zhu (Senior Member, IEEE) received the B.S. degree in computer science and technology from Fudan University, Shanghai, China, in 2003, and the Ph.D. degree in computer engineering from Nanyang Technological University, Singapore, in 2008.

He is currently a Professor with the College of Computer Science and Software Engineering, Shenzhen University, Shenzhen, China. His research interests include computational intelligence, machine learning, and bioinformatics.

Dr. Zhu is an Associate Editor of the *IEEE TRANSACTIONS ON EVOLUTIONARY COMPUTATION* and the *IEEE TRANSACTIONS ON EMERGING TOPICS IN COMPUTATIONAL INTELLIGENCE*. He is also the Chair of the IEEE CIS Emergent Technologies Task Force on Memetic Computing.



Chuen Heung Yau received the bachelor's degree in medicine from the Hunan University of Traditional Chinese Medicine, Hunan, China, in July 1985, and the master's degree in Chinese medicine (acupuncture) from The University of Hong Kong, Hong Kong, in February 2002. She is currently pursuing the Ph.D. degree with the Hunan University of Traditional Chinese Medicine.

She worked as a Doctor with Hunan Provincial Traditional Chinese Medicine Hospital, Hunan, China, from August 1985 to July 1992. She was a Lecturer and Deputy Chief Chinese Medicine Practitioner with the School of Chinese Medicine, Hong Kong Baptist University, Hong Kong, from April 1999 to July 2019. She is currently with the School of Chinese Medicine, The University of Hong Kong, as a Lecturer. She has authored or coauthored 17 articles, one book, and two chapters of the books. The research interest is mainly in the psychoanalysis of children with autism and the observation of the effect of scalp acupuncture on it.



Kay Chen Tan (Fellow, IEEE) received the B.Eng. degree (Hons.) in electronics and electrical engineering and the Ph.D. degree in evolutionary computation and control systems from the University of Glasgow, Glasgow, U.K., in 1994 and 1997, respectively.

He is currently a Full Professor with the Department of Computer Science, City University of Hong Kong, Hong Kong. He has authored or coauthored over 200 refereed articles and six books.

Dr. Tan was an Elected Member of the IEEE CIS AdCom from 2017 to 2019. He currently serves as the Editorial Board Member of over ten journals. He is the Editor-in-Chief of the *IEEE TRANSACTIONS ON EVOLUTIONARY COMPUTATION*. He was the Editor-in-Chief of the *IEEE Computational Intelligence Magazine* from 2010 to 2013.